



Scaling up the cold sintering process of ceramics

Abdullah Jabr^{a,*}, Haley N. Jones^{b,d}, Andrea P. Argüelles^{c,d}, Susan Trolrier-McKinstry^{b,d}, Clive Randall^{b,d}, Raul Bermejo^{a,b}

^a Department of Materials Science, Montanuniversität Leoben, Franz Josef-Strasse 18, A-8700 Leoben, Austria

^b Department of Materials Science and Engineering, The Pennsylvania State University, University Park, PA 16802, USA

^c Department of Engineering Science and Mechanics, Penn State University, University Park, PA 16802, USA

^d Materials Research Institute, Millennium Science Complex, University Park, PA 16802, USA

ARTICLE INFO

Keywords:

Cold sintering
Ultrasonic testing
Strength
Fractography
Scaling up

ABSTRACT

The cold sintering process (CSP) densifies ceramics below 300 °C by utilizing a transient phase and applied pressure. Although CSP has been employed for densifying a variety of functional systems, their structural integrity does not always reach that of conventionally sintered parts. On the example of ZnO, this study aims to eliminate processing-induced defects that compromise the strength of cold sintered materials. Ultrasonic evaluation was employed for nondestructive detection of flaws prior to mechanical testing. Load transfer misalignments and fast heating rates were found as major sources of defects, impairing the mechanical strength. Based on these findings, multiple disc-shaped samples (13 mm diameter and ~1.3 mm thickness) were cold sintered simultaneously using precisely aligned punches and slow heating rates. The obtained homogeneous densification, high relative density (>97%) and relatively high strength (~120 MPa), i.e. two times superior to previously reported values, demonstrates the feasibility of scaling up the CSP towards industrial implementation.

1. Introduction

Sintering of ceramics is conventionally performed at high temperatures above 1000 °C [1,2]. However, due to the increasing demand for advanced multifunctional materials, in addition to the need to support global efforts in environmental sustainability, there is an increasing interest in lowering the sintering temperature. Among the alternative sintering techniques, ultralow-temperature sintering (< 300 °C) has been demonstrated by the cold sintering process (CSP) on a wide variety of ceramics, composites of ceramics, metals and polymers [3–5]. The process is enabled by the simultaneous action of a chemically active transient liquid phase and external pressure to drive densification through particle rearrangement, dissolution and precipitation in a mechanism referred to as pressure solution creep [6]. This substantial reduction in the sintering temperature opens new possibilities for microstructural control, grain boundary engineering [7], processing of thermally unstable materials [8] and co-integration of a wide spectrum of materials, leading to new material development and enhanced functionalities. From a sustainability point of view, a techno-economic analysis has shown that CSP is the most economically appealing option for decarbonizing the ceramic industry [9]. However, one

important shortcoming of CSP is the low amount of material that can be sintered in a single cycle. Hence, scaling up strategies are still needed to establish the CSP as an industrial process for manufacturing ceramic components.

An important property that needs to be considered is the structural integrity of cold sintered materials. The first investigation on the biaxial strength of cold sintered ceramics was on the ZnO system sintered with aqueous solution of zinc acetate [10]. A characteristic strength of ~65 MPa and a Weibull modulus of 8 were reported, which were relatively low compared to conventionally sintered ZnO [10]. Fractographic analyses that explain macroscopic fracture behaviour of cold sintered samples cannot be found in the literature. The only attempts to characterize the fracture behaviour of cold sintered ZnO was performed at the micro-scale using nanoindentation and micropillar testing [11]. The measured hardness and compressive strength were superior to those of conventionally sintered samples and comparable to single crystals. Nevertheless, this study was limited to the microscale, and so may not explain macroscopic mechanical responses controlled by macroscopic defects [12]. Another important aspect of densification and thus the mechanical strength of CSP parts is the transient liquid phase. In a previous work, it was found that high densification can be achieved

* Corresponding author.

E-mail address: abdullah.jabr@unileoben.ac.at (A. Jabr).

<https://doi.org/10.1016/j.jeurceramsoc.2023.04.061>

Received 17 March 2023; Received in revised form 26 April 2023; Accepted 28 April 2023

Available online 29 April 2023

0955-2219/© 2023 The Author(s). Published by Elsevier Ltd. This is an open access article under the CC BY license (<http://creativecommons.org/licenses/by/4.0/>).

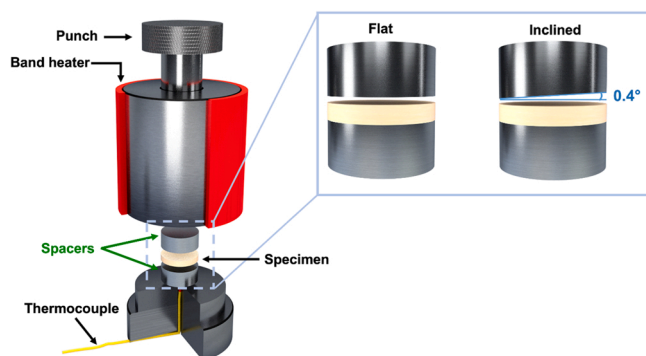


Fig. 1. Experimental setup of the cold sintering process showing the configuration of the flat and inclined upper punch. The temperature of the process is monitored through a thermocouple inserted in the bottom base plate of the sintering die.

(relative density > 95%) when either acetic or formic acid are used [13]. Interestingly, the strength of samples cold sintered with formic acid was found to be twice the strength of samples sintered using acetic acid despite similar densities. Only by using formic acid as a transient liquid phase, the strength was improved by 40% compared to the first reported values on the ZnO system [10]. Thus, the choice of the liquid phase is key to guaranteeing dense and structurally reliable parts.

Given the complex processing conditions in CSP, i.e., application of pressure (typically several hundreds of MPa), heat and evaporation of a transient liquid phase during sintering, processing defects such as delaminations could be induced if the sintering parameters are not chosen correctly. Another aspect is the lack of tools and equipment dedicated for cold sintering. Most experiments are carried out in commercial pressing dies intended for dry powder pressing, which might have insufficient tooling quality, and consequently, result in stress gradients [14]. The occurrence of macroscopic defects associated with CSP has been scarcely addressed in the literature and will be the objective of this paper. Even though mechanical testing combined with fractography is commonly used to establish microstructure–properties relationships, it only reveals the weakest area in the part under the testing load. Therefore, a nondestructive ultrasonic testing method is implemented here; this technique offers a route to detecting flaws and microstructural features throughout the cold sintered parts [15]. Specifically, attenuation measurements have proven to be effective in detecting flaws in parts produced by novel processing techniques, such as additive manufacturing [16,17]. A high attenuation coefficient arises as a result of a decrease in the amplitude of the incident wave due to absorption or scattering of the wave away from its incidence direction, which is typically caused by defects [18]. The sensitivity of attenuation to flaws has been demonstrated in previous works [16,17]. In this paper, an optimization study was carried out with the aim of identifying and eliminating sources of microstructural defects in cold sintered parts, to establish the fundamentals for scaling up of the CSP for ceramics.

2. Experimental procedure

2.1. Materials and cold sintering process

Cold sintering experiments were conducted using ZnO powder with particle sizes between 40 and 100 nm (Alfa Aesar NanoArc™ ZN-0605). The transient liquid phase was a 2 mol/L aqueous solution of formic acid prepared by diluting the concentrated acid (reagent grade $\geq 95\%$, Sigma-Aldrich®) with pure deionized water. This concentration was selected based on a previous work reporting enhanced densification under CSP at an acid concentration of 2 mol/L [19]. Formic acid was selected based on a previous study showing improved mechanical strength and densification behaviour over other liquid phases [13].

Table 1

Summary of the processing conditions of the different cold sintered samples and their corresponding labels.

Sample label	Pressure [MPa]	Temperature [°C]	Heating rate [°C/min]	Dwell time [h]	Quality of the die
CSP \perp		70	10	1	Inclined
CSP \angle		70	10	1	Inclined
CSP1	335	125	1	0	Surface flat
CSP10		125	10		
CSP30		125	30	1	

Samples were fabricated by mixing 1.0 g of ZnO powder with 13 wt% of 2 mol/L formic acid in an agate mortar and pestle. Subsequently, the mixed powder was filled into a pressing die with a diameter of 13 mm. The process was started by applying a pressure of 335 MPa (ENERPAC® semiautomated press) at room temperature for 5 min, followed by heating to the target temperature. The heating rate was set at 1, 10 or 30 °C/min, depending on the experiment. The corresponding samples are labelled hereinafter as CSP1, CSP10 and CSP30. The temperature was controlled by a thermocouple inserted in the bottom of the base plate of the die as depicted in Fig. 1. The effect of the heating rate was studied at a target temperature of 125 °C. To investigate the effect of the tooling quality, the cold sintering temperature was set at 70 °C. This temperature was selected to minimize temperature gradients, which may overshadow the effects produced by the different tooling sets. Based on a previous study [13], rapid evaporation of the liquid phase and maximum shrinkage rate was observed to occur at ~ 85 °C [13]. Therefore, a cold sintering temperature of 70 °C is low enough to reduce the effect of temperature gradients and rapid liquid phase evaporation. Despite the low relative density of $\sim 80\%$ after cold sintering at this temperature, the CSP imparted the samples sufficient integrity for further handling. The effect of tooling quality on the homogeneity of pressure application was investigated by measuring flatness deviation on a commercial pressing die in the as-received state. As depicted in Fig. 1a, the die set consists of a punch and two spacers between which the powder is pressed. To measure the relative inclination of the tools' surfaces, a position measurement unit (Heidenhain ND280) with an accuracy of ± 1 μm was used. The as-received spacers were out of flatness and had a height difference of ~ 40 μm across the diameter, giving a total inclination of ~ 80 μm in the worst-case orientation. Parallel and angle polishing was performed using a Multiprep™ Polishing System, which allows precise polishing with 5 μm accuracy. All parts of the die set (the punch and spacers) were ground and polished to 4000 grit finish to flat surfaces with flatness deviation < 5 μm . However, for a systematic study one spacer was polished with a deviation of 80 μm which corresponds to an inclination angle of $\sim 0.4^\circ$. This spacer was used on the top side of the sample in selected experiments (see Fig. 1). Samples cold sintered using flat or inclined top spacers are hereinafter referred to as CSP \perp and CSP \angle , respectively. A summary of the processing conditions of the different samples is shown in Table 1.

The density was evaluated according to EN 1389:2003 [20] using the Archimedes method with distilled water as the immersion liquid. For samples with open porosity (relative density < 90%), the density was measured geometrically.

2.2. Scaling up experiments

The same powder preparation method described in Section 2.1 was used for the scaling up experiments, except that a larger amount of 5.0 g ZnO powder was initially mixed with the liquid phase in a ratio of 13 wt % for the preparation of 5 samples. All batches were prepared under controlled ambient conditions at a relative humidity of $\sim 40\%$ and a temperature of ~ 22 °C. After optimizing the processing conditions on the small scale, cold sintering of five specimens in one cycle was carried out in a custom-designed die (KEKO Equipment, Slovenia). This die had

a height of 150 mm to allow for the processing of multiple samples in a serial configuration (stack) and a cavity size of 13 mm to produce samples with the same dimensions as those in the optimization study. The samples were separated by stainless steel spacers with a height of 12 mm and a surface flatness accuracy within 5 μm . Heat and pressure were applied by an automatic hydraulic press (TRP-CSP, KEKO Equipment, Slovenia). The applied pressure was 200 MPa (single-action mode). Due to the different temperature probing positions in both setups, the sintering temperature in the scaled-up configuration was set to 140 $^{\circ}\text{C}$ to match the temperature of 125 $^{\circ}\text{C}$ on the small scale. This temperature was chosen based on calibration measurements performed using a thermocouple inserted in the center of the cavity (see Fig. S1 in supplementary information). Due to the difference in the die/punch clearance in this setup compared to the small die, a heating rate of 5 $^{\circ}\text{C}/\text{min}$ was found to be appropriate to produce homogeneous samples.

2.3. Ultrasonic testing

Among the different NDT methods, ultrasonic testing (UT) has gained a growing interest as a quality control tool, finding increasing application in the characterization of materials manufactured through novel processing techniques, such as additive manufacturing [21]. UT relies on transmitting acoustic waves through the material and measuring changes in acoustic parameters caused by the interaction of the acoustic wave with microstructural characteristics of the material.

By monitoring these changes, material properties such as porosity [22], elastic constants [23], and grain size [24] can be inferred. Wave speed is related to the elasticity and density of the material, and therefore, can be used to locally identify porosity [25,26]. On the other hand, attenuation is a result of amplitude reduction of the incident wave caused by absorption or scattering from the incidence direction, which occurs at defects and microstructural heterogeneities [18]. Previous studies have demonstrated the utility of ultrasonic attenuation measurements for flaw-detection and prediction of failure origin, where high attenuation values correspond to defective sites [17,27,28].

In this study, each sample was nondestructively characterized via ultrasonic testing prior to mechanical testing. Ultrasonic testing was conducted using a custom water immersion ultrasonic system (Mistras Group, Princeton Junction, NJ). The ultrasonic test setup is shown elsewhere [15]. A JSR DPR500 pulse receiver 219 (Pittsford, NY) was used to excite and receive ultrasonic waves and an AD8xGDAQ card digitized the waveforms. An Olympus A317 spherically focused transducer (nominal center frequency: 20 MHz, element diameter: 6.35 mm, focal length: 50.8 mm) at normal incidence to the sample surface was raster scanned with a resolution of 0.25 mm. Samples were placed in a water-filled tank on 6.35 mm steel standoffs on a leveling plate to ensure the sample surface and transducer were normal to each other and only longitudinally polarized waves propagated in the solid. The average of ten waveforms was collected at each scanning position using a 1000 MHz sampling rate. Samples with open porosity (relative density

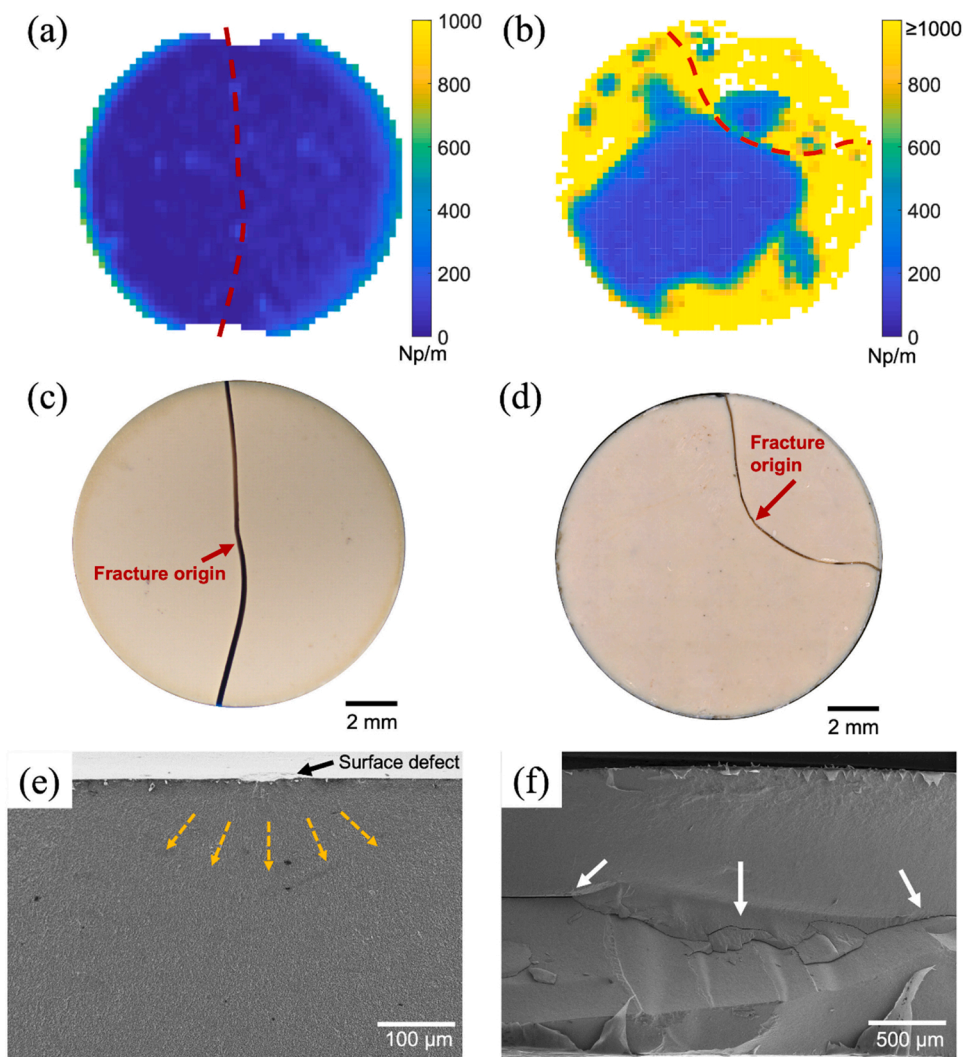


Fig. 2. Fracture behaviour of samples cold sintered at 70 $^{\circ}\text{C}$ using (a, c, e) flat and (b, d, f) inclined punch: Ultrasonic attenuation maps of (a) CSP_{\perp} and (b) CSP_{\angle} . The dashed line represents the fracture path as observed on the tensile side of the specimen. The fracture pattern is displayed by the stereomicroscope image of the tensile side of (c) CSP_{\perp} where the fracture origin is in the center and (d) CSP_{\angle} with off-center fracture origin. SEM micrographs of the fracture surface of (e) CSP_{\perp} where a surface defect was identified as the fracture origin, and (f) CSP_{\angle} showing a large delamination across the fracture surface. Both samples had a relative density of $\sim 80\%$. The top side of the specimen in (e) and (f) is the tensile side.

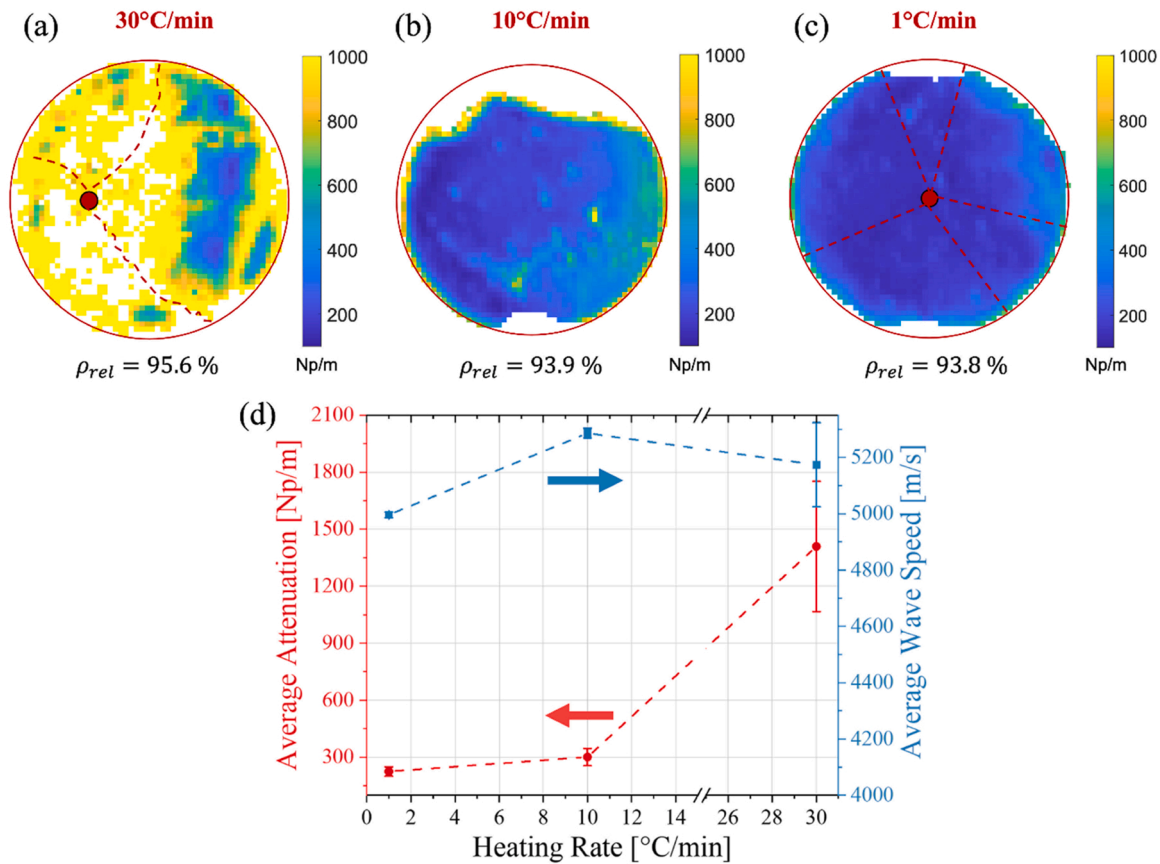


Fig. 3. Ultrasonic attenuation maps measured on CSP30, CSP10 and CSP1 cold sintered at a heating rate of (a) 30 °C/min, (b) 10 °C/min and (c) 1 °C/min, respectively. The red circle indicates the perimeter of the specimen. (d) average attenuation and wave speed versus the heating rate in CSP. The red dots and dashed lines in (a, c) denote the fracture origin and fracture path, respectively, as localized by the fractographic analyses in Fig. 4.

< 90%) were coated with ~5 μm of parylene prior to immersion to reduce water infiltration of the pores.

Thickness independent longitudinal wave speed (c_m) was calculated as:

$$c_m = \left(\frac{T_w - T_m}{T_2 - T_1} + 1 \right) c_w \quad (1)$$

where T_m is the time of flight from the reflector, T_w is the time of flight from the reflector without the sample present along the propagation path, T_2 is the time of flight from the bottom surface of the sample, T_1 is the time of flight from the top surface of the sample, and c_w is the experimentally measured wave speed of the water. The thickness independent longitudinal wave speed was used to accurately determine the thickness (t_s) across the sample area in order to quantitatively calculate the sample attenuation (α_s) by:

$$\alpha_s(f) = -\frac{1}{2t_s} \ln \frac{|\Gamma_s(f)|(1 - R_{ref}^2)R_{ref}}{|\Gamma_{ref}(f)|(1 - R_s^2)R_s} + \alpha_w(f) \frac{WP_{ref} - WP_s}{t_s} \quad (2)$$

where t_s is the sample thickness at each scanning position, $|\Gamma_s(f)|$ and $|\Gamma_{ref}(f)|$ are the spectral amplitudes of the back surface reflections for the reference silica and each scanning point on the sample, respectively, and R_s and R_{ref} are the sample and reference silica reflection coefficients, respectively, calculated using the experimentally measured wave speeds. α_w is the attenuation in the water (10.1 Np/m), which is determined by $\alpha_w = 25.3 \times 10^{-15} f_c^2$ with f_c being the transducer center frequency, and WP_s and WP_{ref} are the water paths for the sample and reference silica, respectively; the water path is defined as $WP = F - (t_s * (c_m/c_w))$ with F being the focal length of the transducer in water. Attenuation coefficient (α_s) spatial maps were generated independent of

sample thickness in MATLAB (2018b) at 12 MHz using the method described in Jones et al. [15] and Cook et al. [16] using fused silica as reference (density 2214 kg/m³, wave velocity 6000 m/s, thickness 1.58 mm).

2.4. Strength and failure analysis

The strength was measured under biaxial bending using the ball-on-three-balls (B3B) test [29,30]. All tests were performed at ambient conditions (~22 °C and ~30% relative humidity) using a Zwick 010 testing machine (Zwick GmbH & Co. KG, Ulm, Germany) with a 10 kN load cell at a displacement rate of 0.5 mm/min and a preload of 5 N. All samples had a diameter of 13 mm and a thickness ranging between 1.2 and 1.4 mm. These were tested in a B3B testing fixture with all four balls having a size of 9 mm. In the B3B test, the tensile stress field is induced in a three-fold symmetry with the maximum tensile stress occurring in the center of the sample. Hence, the homogeneity of the samples could be inferred by fractographic analyses, such that off-center fracture is a sign of inhomogeneous defect distribution. The strength results were evaluated according to the two-parameter Weibull statistics using the maximum likelihood method and following the standard EN-843-5 [31]. Fractography was conducted using a stereomicroscope (Smartzoom 5 digital microscope, Carl Zeiss Microscopy LLC., United States) and a scanning electron microscope (Thermo Scientific™ Apreo 2 SEM). Fracture surfaces were coated with a 5 nm layer of iridium using a sputter coater (Leica EM ACE600).

2.5. Thermogravimetric Analysis (TGA)

TGA was conducted to determine the amount of residual organic

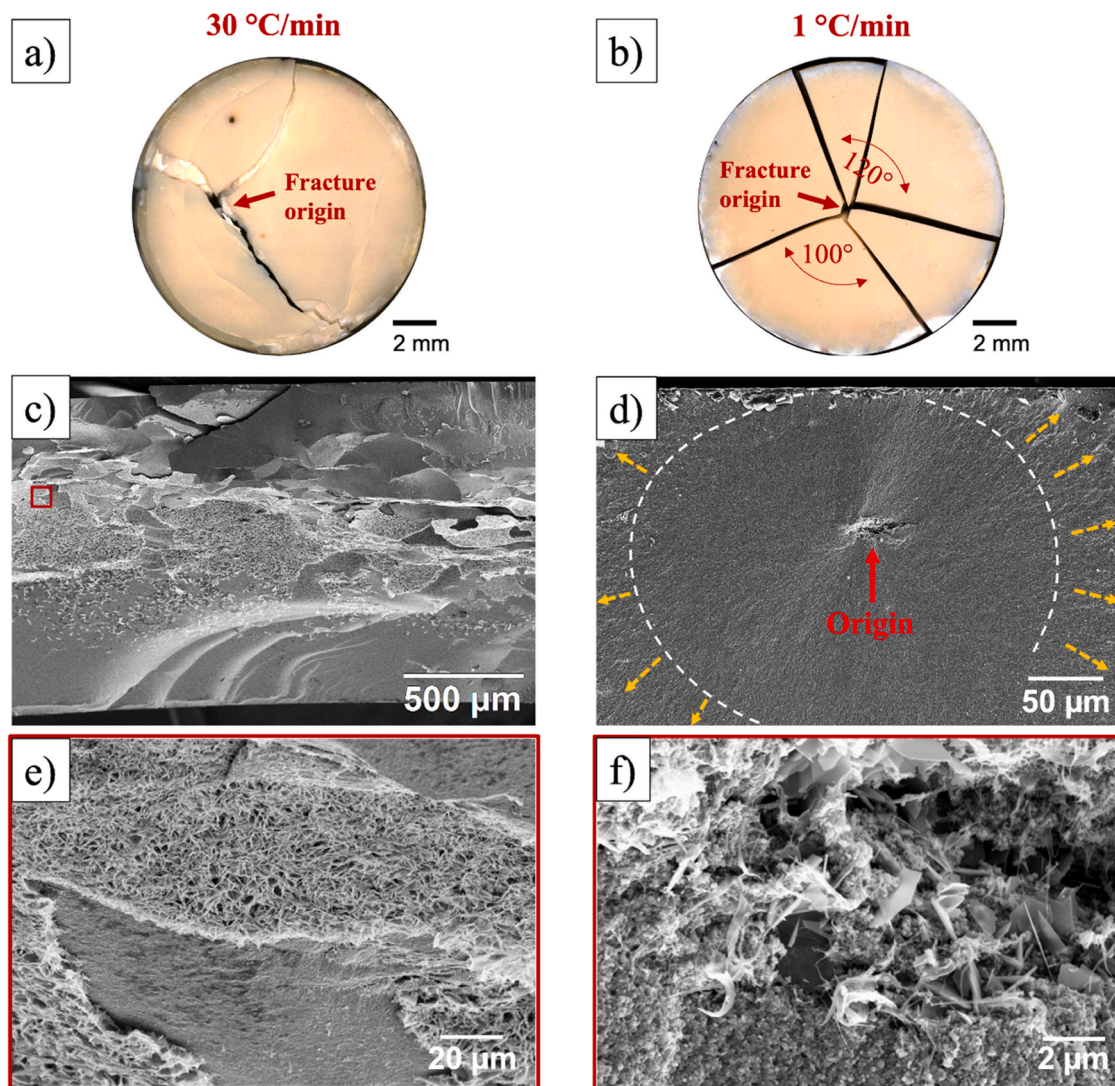


Fig. 4. Fracture behaviour of CSP30 (left column) and CSP1 (right column): Stereomicroscope images showing the fracture pattern on the tensile side of (a) CSP30 and (b) CSP1. Fracture surface and enlarged view of fracture origin in (c,e) CSP30 and (d,f) CSP1. The white dashed line in (d) indicates the fracture mirror. The strength values of CSP30 and CSP1 were 24 and 87 MPa, respectively. The top side of the specimen in (c) and (d) is the tensile side.

content in samples produced by the scaled-up process. All measurements were performed using a thermal analyser (Mettler Toledo TGA/DSC 3 +) in a temperature range between 20 and 600 °C with a heating rate of 5 °C/min under nitrogen atmosphere. The samples were analysed in a crushed form with a mass of ~ 20 mg.

3. Results and discussion

3.1. Effects of tooling misalignment

The effect of misalignment in the pressing system was investigated by conducting cold sintering experiments using inclined and precisely machined flat punches, as depicted in Fig. 1. The results are compared with respect to densification homogeneity, which is enabled by ultrasonic testing, as well as mechanical response. The homogeneity of the microstructures was inspected through nondestructive ultrasonic testing using longitudinal waves (Fig. 2a and b). Fig. 2a shows a longitudinal ultrasonic attenuation map of a sample cold sintered with a flat punch, where homogeneous load transfer is expected. As can be seen, CSP \perp has a homogeneous map with low attenuation coefficient, showing (initial) densification without microstructural discontinuities or macroscopic defects. The fracture of this sample initiated in the center (Fig. 2c),

where the maximum biaxial tensile stress in the B3B-test is expected [29]. This is further evidence for the homogeneity of the microstructure. Fig. 2e shows the fracture surface of the sample, depicting a surface flaw as the fracture origin.

The effect of improper load transfer into the powder compact during cold sintering is revealed by the attenuation map in Fig. 2b. In CSP \angle , attenuation is lowest at the central region and increases remarkably toward the edge of the sample. Regions of high attenuation indicate the presence of defects scattering the ultrasonic waves. The mechanical response correlates well with the location of the defects in the attenuation map, as depicted by the off-center fracture origin (Fig. 2d). In this case, fracture occurred along the interface between the homogeneous and the flawed region as shown by the attenuation map. The fracture surface is shown in Fig. 2f, where a delamination crack acted as fracture origin. These deleterious effects of tooling misalignment may be attributed to pressure gradients and additional shear stresses in the compact, which could ultimately lead to delaminations. Cracking may also evolve during pressure release and/or ejection from the die. Previous work has shown through finite element simulations that a combination of shear and tensile stresses are induced as the compact is ejected from the pressing die, leading to cracking and subsequent failure of the part [14,32]. These stresses could be expected to be accentuate

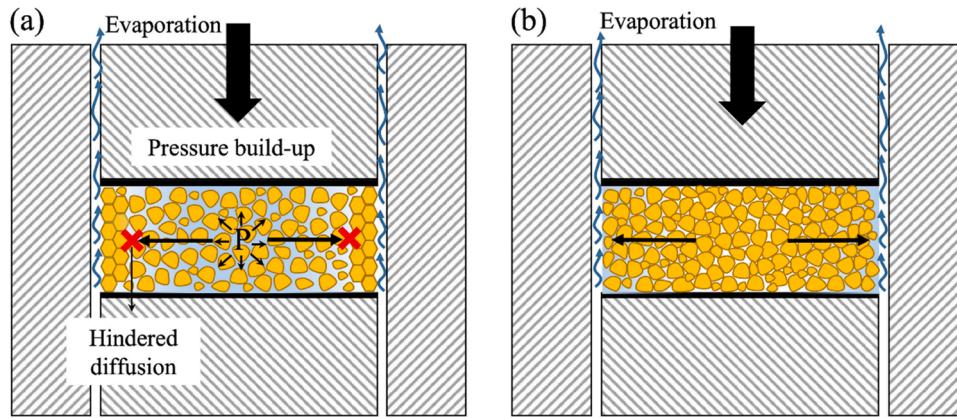


Fig. 5. Schematic representation for the effect of heating rate on densification homogeneity: (a) CSP with fast heating rate, where the densified edge hinders removal of the liquid phase. (b) CSP with slow heating rate, allowing homogeneous liquid phase removal and densification.

under nonuniform load transfer.

The occurrence of such pressure inhomogeneities should not be underestimated, as it is not only limited to the quality of the punch but can also be induced by misalignment of the press. It is also a common practice in CSP experiments to polish damaged or corroded punches, which could potentially introduce such inclinations in the system if care is not taken to this point. These results highlight the importance of ensuring uniform load transfer, which is dictated by the tooling quality of the punch, as well as the different parts of the pressing system.

3.2. Effects of heating rate

The next step after eliminating inhomogeneities caused by improper tooling quality is to drive full densification by considering temperature effects. Full densification requires CSP temperatures above 90 °C to evaporate the liquid phase and drive the pressure solution creep mechanism [13]. Fig. 3 shows the effect of the heating rate on the homogeneity of cold sintered samples as depicted by the ultrasonic attenuation maps. As can be seen from Fig. 3a, the fast-heating rate used in CSP30 resulted in pronounced gradients in the measured attenuation with high attenuation values observed over large parts of the specimen. These high attenuation values are associated with the presence of abundant microstructural discontinuities and defects, which act as scattering sites for the incident waves. The missing data in the center of the specimen is caused by the loss of reflected ultrasonic waves due to intense scattering. The attenuation map of CSP10 shows that decreasing the heating rate from 30 °C/min to 10 °C/min reduces the spatial attenuation coefficient in large areas of the specimen (Fig. 3b). However, some defects can still be detected, specially toward the edges. As displayed in Fig. 3c, a slow-heating rate of 1 °C/min resulted in a uniform attenuation map with very low attenuation coefficient values, indicating that slow heating rates are beneficial for reducing defects and heterogeneities in cold sintered materials. Fig. 3d shows the average measured attenuation and wave speed (the average of all measured values across the specimens) as a function of heating rate. As can be seen, the average attenuation correlates positively with the heating rate. The increase in scatter with heating rate is attributed to the increased degree of inhomogeneity. In contrast to CSP30, which fractured off-center in the region with the highest attenuation, the fracture in CSP1 initiated at the center of the specimen where the highest biaxial tensile stress is expected in the B3B test, indicating improved homogeneity for CSP1. Moreover, a direct influence of the heating rate on the density was not observed, as the difference in the relative densities between the different heating rates was less than 2%. This is also evident from the average ultrasonic wave speed in Fig. 4d, which shows negligible effect of the heating rate (the values of CSP1 and CSP10 are within the range of measured values of CSP30, being between 4847 and

5145 m/s).

To reveal the nature of defects detected by the ultrasonic attenuation measurements, fractographic analyses were carried out on the two extreme cases: CSP30 and CSP1. Fig. 4a shows the fracture pattern observed on the tensile side of CSP30, where the fracture origin is located at the region of highest measured ultrasonic attenuation. In addition, the fracture path follows regions of missing attenuation data which are expected to correspond to highly defective areas based on the loss of reflected waves (cf. red markings in Fig. 3a). The torturous crack path is a result of crack propagation along weak regions in the microstructure as revealed by the attenuation map. In contrast, the fracture in CSP1 initiated by cracking in the center, which branched in multiple straight cracks (Fig. 4b). It is well known that the branching angle is indicative of the stress state endured by the sample [33]. In this case, the branching angle was between ~100° and ~120°, corresponding to a biaxial stress state as expected in the B3B test. This remarkable difference in the degree of homogeneity between the specimens translates into a large difference in the measured strengths, being 24 MPa for CSP30 and 87 MPa for CSP1. These results show that ultrasonic testing can be used to predict the location of defects and weak sites in the microstructure, i.e., fracture origin and favourable crack propagation paths.

The fracture surface of CSP30 consists of multiple cracks and delaminations, which are the source for the high attenuation values and the low strength measured on this specimen (Fig. 4c). Moreover, a large area of the fracture surface is covered by a flake-like morphology (Fig. 4e). Such morphology was observed frequently on fracture surfaces and inside crack wakes. This may indicate that the growth of this morphology is related to the entrapment of the liquid phase within the microstructure, which can lead to pressure build up with temperature increase, and therefore, cracking. On the other hand, the fracture surface of CSP1 shows a homogeneous microstructure with typical fractographic features as commonly encountered in well densified materials, i.e., a fracture origin surrounded by fracture mirror and hackle lines (Fig. 4d). The fracture origin is identified as a subsurface inhomogeneity, consisting of a flake-like phase, which can be attributed to nonuniform distribution of the liquid phase, causing its entrapment within small regions (Fig. 4f).

Flake-like ZnO crystals have been observed in previous studies on the growth of ZnO under hydrothermal conditions [34–36]. Based on the reported morphological characteristics of these crystals it can be deduced that the observed formation of cracks in CSP30 might be related to the occurrence of local hydrothermal conditions due to the entrapment of the liquid phase. Local hydrothermal conditions in the bulk may occur if the liquid phase is entrapped by the surrounding densifying microstructure before evaporation, which is expected if the material is densifying inhomogeneously. This is anticipated to occur when a fast-heating rate is used, which may result in different densification rates

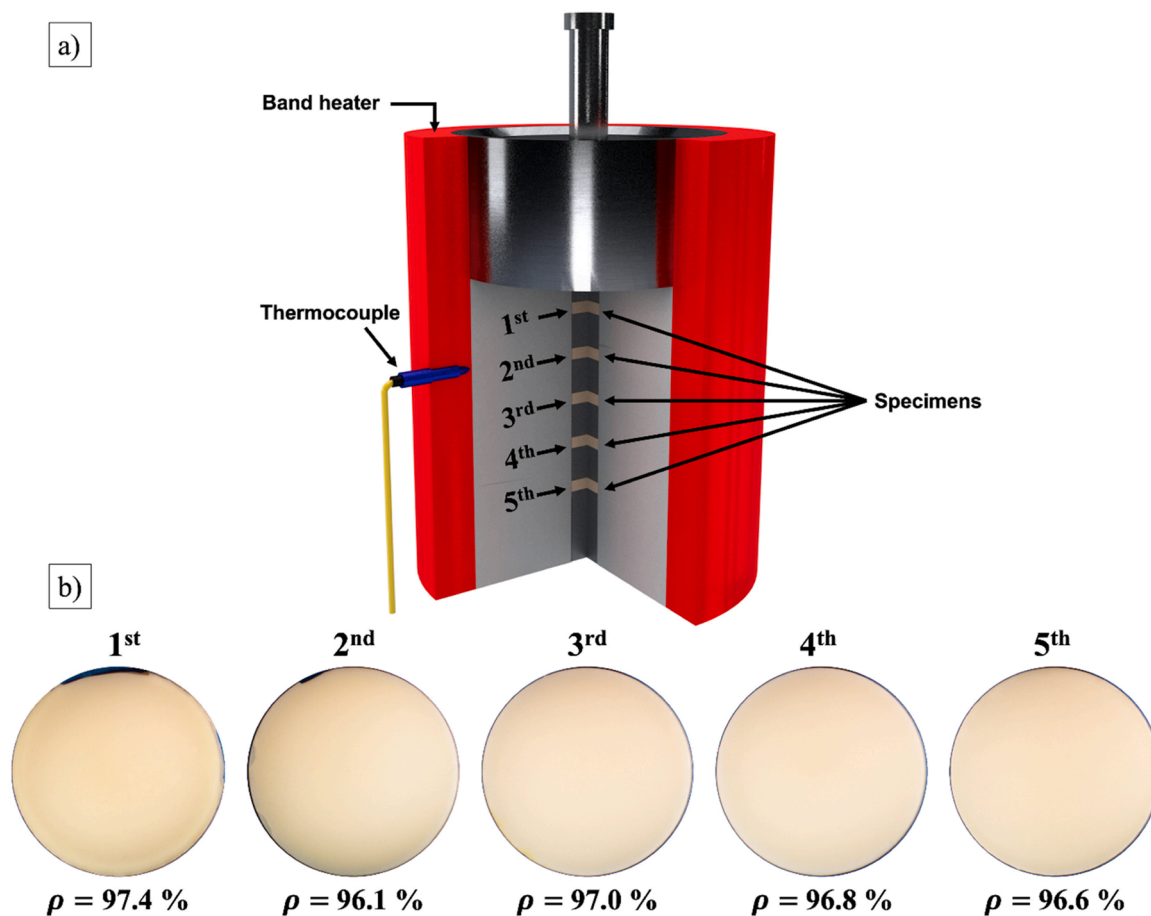


Fig. 6. (a) Schematic of the scaled-up cold sintering setup showing the thermocouple probing position, band heater and the position of each sample denoted in ordinal sequence. (b) Stereomicroscope image of the physical appearance of a representative set of samples after cold sintering at ~ 125 °C for 1 h. The relative density, ρ , of each specimen is inserted below its image.

between the edge and the center of the specimen. In CSP, heat is typically applied through a heating jacket wrapped around the sintering die. In such a setup, the heat flows radially from the heating elements through the die and into the sample. This may result in a temperature gradient within the sample if the rate of heat flow is not adequately selected, which can be controlled by adjusting the heating rate during the anisothermal stage of CSP. This is indeed in agreement with the observed increase in ultrasonic attenuation (defect density) with heating rate (Fig. 3), where CSP30 showed signs of hydrothermal growth of ZnO crystals that were correlated with cracking. The difference in the densification rates between the edge and the center of the specimen at fast heating rates might be explained by: (a) a temperature gradient within the specimen, causing the perimeter to reach the CSP temperature faster than the center, and (b) a longer diffusion distance for the liquid phase in the center of the specimen relative to the edge region (Fig. 5).

Overall, these results indicate that the optimal heating rate in CSP should provide a balance between the kinetics of pressure solution creep and liquid phase evaporation throughout the specimen. It should be noted that the optimal heating rate may change depending on the size of specimen, the tolerance between the punch and die (clearance), powder characteristics and the initial compaction behaviour (pore-network connectivity). The die clearance of the pressing system has been reported to remarkably affect densification under CSP [37].

3.3. Scaling up the cold sintering process

Scaling up the CSP from one-piece per cycle into a batch process will

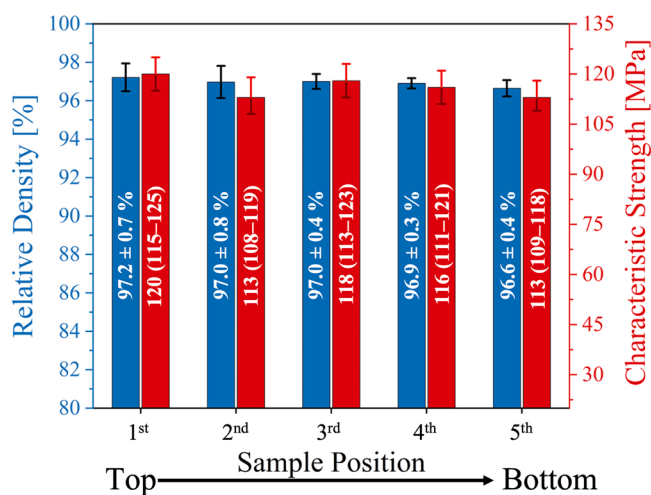


Fig. 7. Average density and characteristic strength for each sample position in the scaled-up CSP. Average densities were calculated from 11 samples per position, along with the corresponding \pm one standard deviation represented as error bars. The characteristic strength was evaluated from at least 15 samples. The error bars of the characteristic strength values represent the corresponding 90% confidence interval.

Table 2

Characteristic strength (σ_0) and Weibull modulus (m), along with the corresponding 90% confidence intervals for each sample position in the scaled-up configuration.

Sample position	Number of tested specimens	Characteristic strength, σ_0 [MPa]	Weibull modulus, m [-]
1st	17	120 (115–125)	11 (7–14)
2nd	16	113 (108–119)	11 (7–14)
3rd	16	118 (113–123)	11 (7–14)
4th	17	116 (111–121)	10 (7–13)
5th	15	113 (109–118)	13 (8–17)

be shown in this section. The setup was modified to allow for the processing of multiple samples in a serial configuration as shown in Fig. 6a. The samples were separated by stainless steel spacers. These were precisely machined to a flat surface with flatness deviation < 5 μm to reduce misalignment effects and promote homogeneous densification. Fig. 6b shows a representative set of samples cold sintered simultaneously in one cycle, displaying identical physical appearance and similar relative densities with less than 1% variation.

The average relative density and characteristic strength of samples cold sintered in the scaled-up configuration at different positions (from the 1st to 5th) are given in Fig. 7. In terms of densification, no remarkable difference could be observed between the samples. In order to assess the equivalence of the average densities of the samples at all positions, a single-factor analysis of variance (ANOVA) was conducted. The normality of the density values was verified by the Kolmogorov-Smirnov test. The ANOVA results indicated no statistically significant

difference between the average values (F-test = 1.37; $p = 0.26$). Fig. 7 also shows the characteristic strength, σ_0 , corresponding to a probability of failure of ~63%, along with the 90% confidence interval of all samples sintered at different positions in the scaled-up process. As can be seen, no statistically significant difference in the strength could be observed between the different positions as the range of the strength values of all positions is overlapping considering the confidence intervals. All Weibull parameters, i.e., the characteristic strength, σ_0 , and the Weibull modulus, m , which is a measure of the scatter of the strength values, are given in Table 2.

Since all sample sets at different positions within each batch are statistically identical within a 90% confidence level (see Fig. S2 in supplementary information), we may collectively combine all into a single data set. The evaluation of this pooled data set of 81 samples results in a characteristic strength of $\sigma_0 = 116$ (114 – 118) MPa and a Weibull modulus of $m = 11$ (9 – 12). As shown in Fig. 8, the strength follows a Weibull distribution showing a typical behaviour of a Weibull material being controlled by a single failure mode. It is worth noting that the strength of samples produced by this scaled-up CSP was twice the strength of the first reported results on cold sintered ZnO and had a ~40% higher Weibull modulus [10]. The lower scatter in the strength data can be ascribed to the reduced variation between the samples within each batch compared to the manual CSP, as these samples were processed using the same powder mixing procedure and sintered in the same cycle. In addition, in manual CSP each sample is prepared by separate powder mixing and sintering step, which makes the process more vulnerable to variations in powder preparation and ambient conditions. The enhanced strength can be related to the higher quality of the

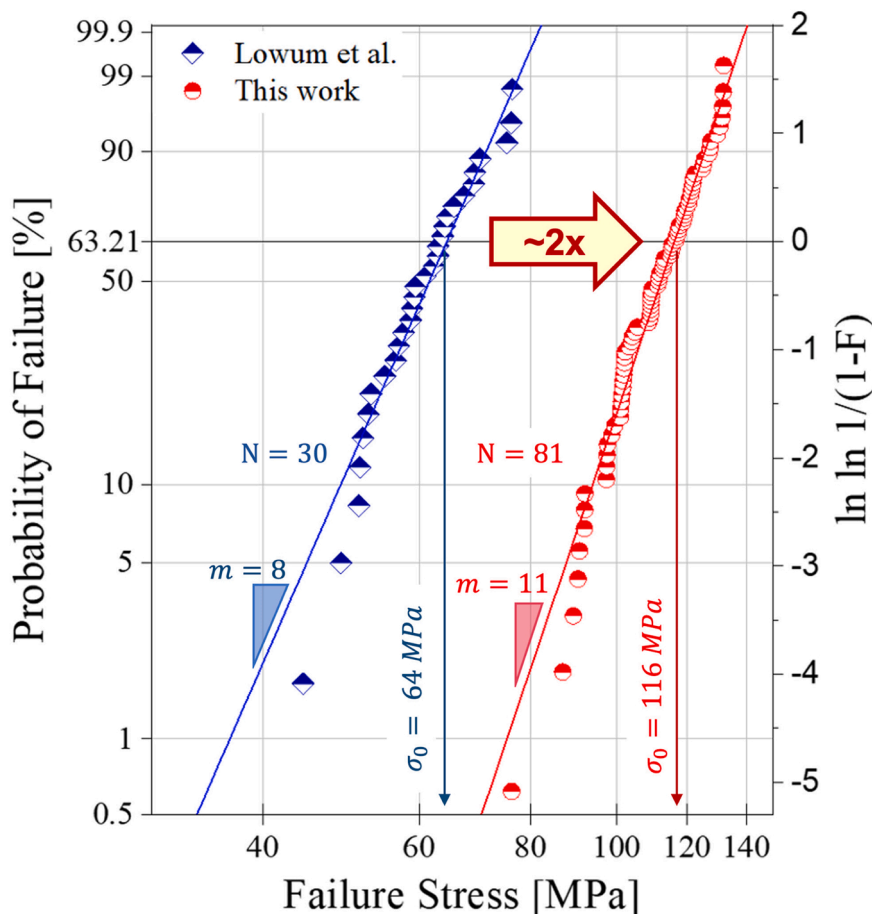


Fig. 8. Weibull plot showing the probability of failure vs. failure stress for cold sintered ZnO using the scaled-up CSP (this work) and compared to the first reported results by Lowum et al. [10]. The number of tested specimens, N , the Weibull modulus, m , and the characteristic strength, σ_0 , of each set are inserted at the corresponding distribution. The solid lines are lines of best fit of the strength data according to the maximum likelihood method.

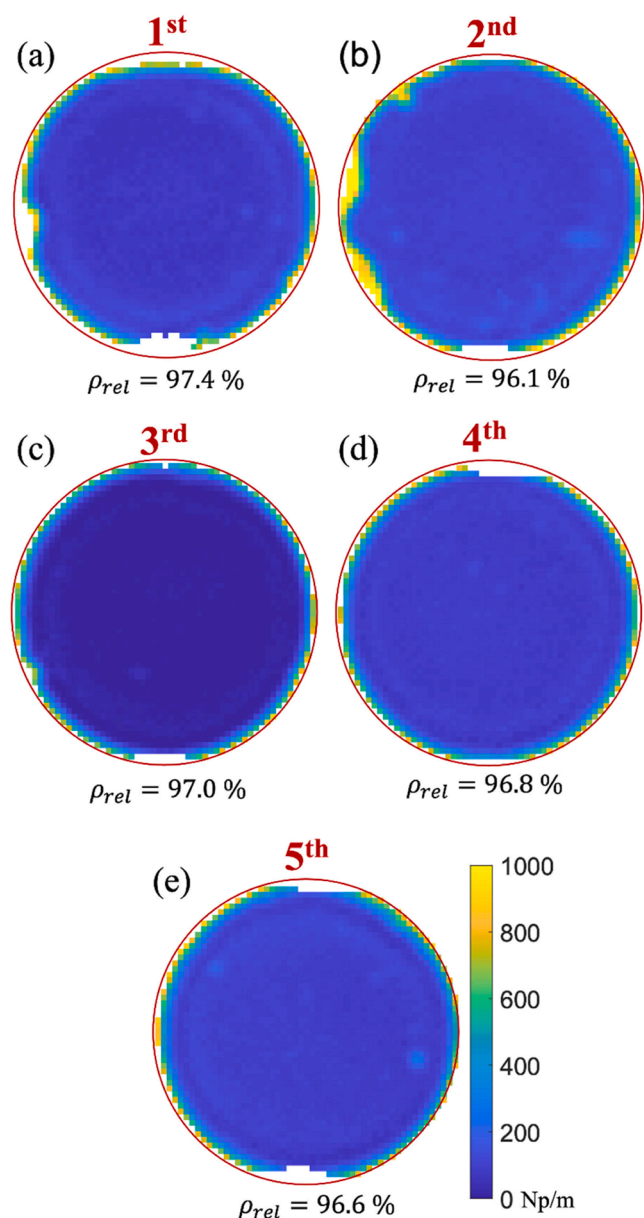


Fig. 9. Ultrasonic attenuation maps of a representative set of samples densified using the scaled-up CSP at different axial positions: (a) 1st (top sample), (b) 2nd, (c) 3rd, (d) 4th, and (e) 5th (bottom sample). The legend in (e) is valid for all maps.

pressing system (fully automated press and precisely machined parts), and/or better pressure redistribution across the samples.

To assess the homogeneity of densification, ultrasonic attenuation measurements were carried out on a set of samples cold sintered in the scaled-up configuration as shown in Fig. 9. Low attenuation values were detected across the area of all samples, indicating homogeneous densification at all positions within the batch. Small regions in samples sintered in the 1st and 2nd positions (Fig. 9a and b) had relatively higher attenuation values, which is speculated to be associated with edge defects generated during ejection of the samples. This takes place from the bottom of the die. Hence, samples in positions 1 and 2 undergo a longer ejection distance compared to samples at lower positions, subjecting the edges to die wall friction. The effect of die wall friction on the pressure distribution within the compact has been reported in previous works [38].

Fig. 10 compares the ultrasonic response of samples produced by the

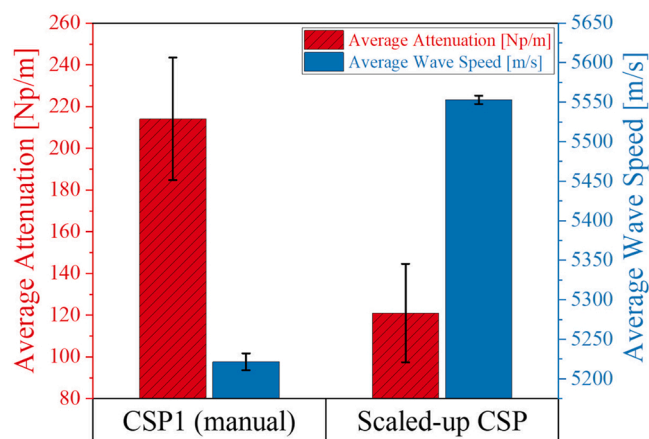


Fig. 10. Average measured ultrasound parameters of the manual (CSP1) versus scaled-up CSP.

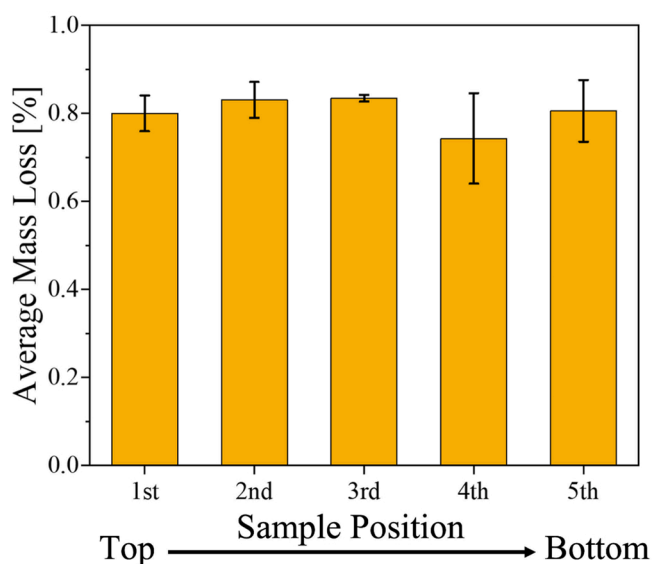


Fig. 11. Average total mass loss measured by TGA of samples sintered in different positions in the scaled-up setup. Error bars represent \pm one standard deviation measured from at least 3 samples.

manual and the scaled-up CSP. The measured attenuation values on samples sintered in the scaled-up process are on average \sim 50% lower than those measured on CSP1, indicating more homogeneous densification in the scaled-up CSP. Regarding wave speeds, an increase in the scaled-up samples was observed, which is related to their higher relative densities (\sim 97% vs \sim 94%). This is consistent with previous studies, which reported a proportional relationship between density and acoustic wave speed [17,26]. These results show that scaling up the CSP is a viable approach to improve the mechanical properties of cold sintered materials and increase the efficiency of CSP.

Another important consideration in the CSP is the release of the liquid phase from the densifying powder through the die clearance. Maier et al. showed by an *in-situ* observation of the CSP of ZnO, using a high aspect ratio length to diameter transparent quartz cavity, that the liquid and vapor phases escape from the edge of the sample and through the die capillary toward the top of the pressing system [39,40]. This could, in principle, result in different residual organic content between the samples in the scaled-up process, such that bottom samples “contaminate” upper samples. However, this phenomenon was not observed to occur as demonstrated by the TGA results in Fig. 11. All

samples showed the same amount of residual liquid phase of ~0.8%, which is in agreement with the previously reported value on cold sintering using formic acid [13].

In summary, the proposed approach of scaling up the CSP using a serial configuration for densifying multiple samples has been successfully demonstrated. All samples within each sintered batch showed identical properties without any gradients or trends between top and bottom positions, i.e., equivalent density, mechanical strength, and residual liquid phase content. Owing to the optimized processing conditions, which reduced temperature gradients and misalignment effects, high homogeneity with a reduced number of defects in all samples was confirmed by ultrasound measurements. This scaled-up process produced samples with enhanced strength and densification compared to the commonly used manual CSP. We regard this as an important first step in considering engineering and scientific challenges of manufacturing with the CSP, and systematically identifying critical process parameters, metrologies, and mechanical property correlations beyond the density and microstructural evolution.

4. Conclusions

In this paper, the occurrence of processing defects under the CSP was investigated. Nondestructive ultrasound measurements followed by mechanical testing and fractographic analyses revealed that pressure transfer uniformity (tooling quality) and heating rate are key factors controlling the homogeneity and strength of cold sintered samples. Misalignment effects induced by improper tooling quality resulted in delamination cracks, which were successfully prevented by using precisely machined flat punches. Moreover, the amount of inhomogeneities in the microstructure was found to correlate with the heating rate, as detected by ultrasonic attenuation measurements. These inhomogeneities were found to be microstructural discontinuities (cracks), presumably generated by densification gradients within the material, which drastically impaired the structural integrity of the cold sintered samples (~70% strength reduction). Homogeneous and structurally reliable cold sintered samples were produced using a slow heating rate and properly aligned compression punches. Based on these optimized cold sintering conditions, the feasibility of scaling up the CSP by sintering five samples simultaneously was demonstrated in a serial configuration. All samples within each batch showed equivalent properties in terms of density (~97%) and mechanical strength (up to ~120 MPa). Ultrasound measurements confirmed the homogeneity of all samples and revealed lower attenuation and higher wave speed values compared to the manual process. This reflected in a two times higher mechanical strength compared to previously reported results using the manual CSP on the ZnO system. This scaled-up process further increases the efficiency and productivity of CSP, towards its industrial implementation as a sustainable alternative sintering technique.

CRedit authorship contribution statement

Abdullah Jabr: Writing – original draft, Conceptualization, Designed and performed the cold sintering and mechanical experiments, Investigation, Formal analysis, Visualization. **Haley N. Jones:** Ultrasound measurements, Formal analysis, Editing. **Andrea P. Argüelles:** Editing, Supervision, Funding acquisition. **Susan Trolier-McKinstry:** Editing, Supervision, Funding acquisition. **Clive Randall:** Editing, Supervision, Conceptualization, Funding acquisition. **Raul Bermejo:** Editing, Supervision, Conceptualization, Validation, Project administration, Funding acquisition.

Declaration of Competing Interest

The authors declare that they have no known competing financial interests or personal relationships that could have appeared to influence the work reported in this paper.

Acknowledgments

Funding for this research was provided by the European Research Council (ERC) excellent science grant “CERATEXT” through the Horizon 2020 program under contract 817615. Abdullah Jabr acknowledges the Austrian Marshall Plan Foundation for the financial support during his stay at Penn State university. Clive Randall and Andrea P. Argüelles would like to thank NSF_FMSG (2134643) program for partial support of this work. Eliza Ribul from the Department of Materials Science, Montanuniversitaet Leoben, Austria, is acknowledged for the support in mechanical testing.

Appendix A. Supporting information

Supplementary data associated with this article can be found in the online version at doi:10.1016/j.jeurceramsoc.2023.04.061.

References

- [1] M.N. Rahaman, *Sintering of Ceramics*, Taylor & Francis, 2008.
- [2] R.M. German, Thermodynamics of sintering, in: *Sintering of Advanced Materials*, Elsevier, 2010, pp. 3–32, <https://doi.org/10.1533/9781845699949.1.3>.
- [3] S. Dursun, K. Tsuji, S.H. Bang, A. Ndayishimiye, C.A. Randall, A route towards fabrication of functional ceramic/polymer nanocomposite devices using the cold sintering process, *ACS Appl. Electron. Mater.* 2 (2020) 1917–1924, <https://doi.org/10.1021/acsaem.0c00225>.
- [4] T. Sada, K. Tsuji, A. Ndayishimiye, Z. Fan, Y. Fujioka, C.A. Randall, Highly reliable BaTiO₃-polyphenylene oxide nanocomposite dielectrics via cold sintering, *Adv. Mater. Interfaces* 8 (2021), 2100963, <https://doi.org/10.1002/admi.202100963>.
- [5] L. Paradis, D. Waryoba, K. Robertson, A. Ndayishimiye, Z. Fan, R. Rajagopalan, C. A. Randall, Densification and strengthening of ferrous-based powder compacts through cold sintering aided warm compaction, *Adv. Eng. Mater.* 24 (2022), 2200714, <https://doi.org/10.1002/adem.202200714>.
- [6] A. Ndayishimiye, S.H. Bang, Christopher J. Spiers, C.A. Randall, Reassessing cold sintering in the framework of pressure solution theory, S095522192200749X, *J. Eur. Ceram. Soc.* (2022), <https://doi.org/10.1016/j.jeurceramsoc.2022.09.053>.
- [7] T. Sada, K. Tsuji, A. Ndayishimiye, Z. Fan, Y. Fujioka, C.A. Randall, High permittivity BaTiO₃ and BaTiO₃-polymer nanocomposites enabled by cold sintering with a new transient chemistry: Ba(OH)₂•8H₂O, *J. Eur. Ceram. Soc.* 41 (2021) 409–417, <https://doi.org/10.1016/j.jeurceramsoc.2020.07.070>.
- [8] S.H. Bang, T. Herisson De Beauvoir, C.A. Randall, Densification of thermodynamically unstable tin monoxide using cold sintering process, *J. Eur. Ceram. Soc.* 39 (2019) 1230–1236, <https://doi.org/10.1016/j.jeurceramsoc.2018.11.026>.
- [9] T. Ibn-Mohammed, C.A. Randall, K.B. Mustapha, J. Guo, J. Walker, S. Berbano, S.C. L. Koh, D. Wang, D.C. Sinclair, I.M. Reaney, Decarbonising ceramic manufacturing: A techno-economic analysis of energy efficient sintering technologies in the functional materials sector, *J. Eur. Ceram. Soc.* 39 (2019) 5213–5235, <https://doi.org/10.1016/j.jeurceramsoc.2019.08.011>.
- [10] S. Lowum, R. Floyd, R. Bermejo, J.-P. Maria, Mechanical strength of cold-sintered zinc oxide under biaxial bending, *J. Mater. Sci.* 54 (2019) 4518–4522, <https://doi.org/10.1007/s10853-018-3173-8>.
- [11] K. Nur, M. Zubair, J.S.K.-L. Gibson, S. Sandlöbes-Haut, J. Mayer, M. Bram, O. Guillon, Mechanical properties of cold sintered ZnO investigated by nanoindentation and micro-pillar testing, *J. Eur. Ceram. Soc.* 42 (2022) 512–524, <https://doi.org/10.1016/j.jeurceramsoc.2021.10.011>.
- [12] Ceramics: mechanical properties, in: D. Munz, T. Fett (Eds.), *Failure Behaviour, Materials Selection*, Springer Berlin Heidelberg, Berlin, Heidelberg, 1999, <https://doi.org/10.1007/978-3-642-58407-7>.
- [13] A. Jabr, J. Fanghanel, Z. Fan, R. Bermejo, C. Randall, The effect of liquid phase chemistry on the densification and strength of cold sintered ZnO, *J. Eur. Ceram. Soc.* 43 (2023) 1531–1541, <https://doi.org/10.1016/j.jeurceramsoc.2022.11.071>.
- [14] J.A. Hernández, J. Oliver, J.C. Cante, R. Weyler, Finite element modelling of ejection cracks in powder metallurgy die compaction processes: case study, *Powder Metall.* 55 (2012) 36–44, <https://doi.org/10.1179/1743290111Y.0000000017>.
- [15] H.N. Jones, E. Trautman, J. Maria, S. Trolier-McKinstry, A.P. Argüelles, Assessment of flaws in cold-sintered ZnO via acoustic wave speed and attenuation measurements, *J. Am. Ceram. Soc.* (2023), <https://doi.org/10.1111/jace.19108>.
- [16] O. Cook, N. Huang, R. Smithson, C. Kube, A. Beese, A. Argüelles, Ultrasonic Characterization of Porosity in Components Made by Binder Jet Additive Manufacturing, *ME* 80 (2022) 37–44, <https://doi.org/10.32548/2022.me-04266>.
- [17] N. Huang, O.J. Cook, J.D. Warner, R.L.W. Smithson, C.M. Kube, A.P. Argüelles, A. M. Beese, Effects of infiltration conditions on binder jet additively manufactured stainless steel infiltrated with bronze, *Addit. Manuf.* 59 (2022), 103162, <https://doi.org/10.1016/j.addma.2022.103162>.
- [18] G. Hübschen, Ultrasonic techniques for materials characterization, in: *Materials Characterization Using Nondestructive Evaluation (NDE) Methods*, Elsevier, 2016, pp. 177–224, <https://doi.org/10.1016/B978-0-08-100040-3.00007-9>.

- [19] S.H. Bang, A. Ndayishimiye, C.A. Randall, Anisothermal densification kinetics of the cold sintering process below 150 °C, *J. Mater. Chem. C* 8 (2020) 5668–5672, <https://doi.org/10.1039/D0TC00395F>.
- [20] E. Standards, BS EN 1389:2003 Advanced technical ceramics-Ceramic composites-Physical properties-Determination of density and apparent porosity, www.en-standard.eu/bs-en-1389-2003-advanced-technical-ceramics-ceramic-composites-physical-properties-determination-of-density-and-apparent-porosity/.
- [21] L.W. Koester, L.J. Bond, H. Taheri, P.C. Collins, Nondestructive evaluation of additively manufactured metallic parts, in: *Additive Manufacturing for the Aerospace Industry*, Elsevier, 2019, pp. 401–417, <https://doi.org/10.1016/B978-0-12-814062-8.00020-0>.
- [22] N.B. Podymova, I.E. Kalashnikov, L.K. Bolotova, L.I. Kobleva, Effect of porosity on the statistical amplitude distribution of backscattered ultrasonic pulses in particulate reinforced metal-matrix composites, *Ultrasonics* 108 (2020), 106235, <https://doi.org/10.1016/j.ultras.2020.106235>.
- [23] N.P. Lavery, J. Cherry, S. Mehmood, H. Davies, B. Girling, E. Sackett, S.G.R. Brown, J. Siens, Effects of hot isostatic pressing on the elastic modulus and tensile properties of 316L parts made by powder bed laser fusion, *Mater. Sci. Eng. A* 693 (2017) 186–213, <https://doi.org/10.1016/j.msea.2017.03.100>.
- [24] A.P. Argüelles, J.A. Turner, Ultrasonic attenuation of polycrystalline materials with a distribution of grain sizes, *J. Acoust. Soc. Am.* 141 (2017) 4347–4353, <https://doi.org/10.1121/1.4984290>.
- [25] J.A. Slotwinski, E.J. Garboczi, K.M. Hebenstreit, Porosity Measurements and Analysis for Metal Additive Manufacturing Process Control, *J. Res. Natl. Inst. Stan.* 119 (2014) 494, <https://doi.org/10.6028/jres.119.019>.
- [26] L. Vergara, R. Miralles, J. Gosálbez, F.J. Juanes, L.G. Ullate, J.J. Anaya, M. G. Hernández, M.A.G. Izquierdo, NDE ultrasonic methods to characterise the porosity of mortar, *NDT E Int.* 34 (2001) 557–562, [https://doi.org/10.1016/S0963-8695\(01\)00020-2](https://doi.org/10.1016/S0963-8695(01)00020-2).
- [27] N. Huang, O.J. Cook, R.L.W. Smithson, C.M. Kube, A.P. Argüelles, A.M. Beese, Use of ultrasound to identify microstructure-property relationships in 316 stainless steel fabricated with binder jet additive manufacturing, *Addit. Manuf.* 51 (2022), 102591, <https://doi.org/10.1016/j.addma.2021.102591>.
- [28] L.D. Sotelo, H. Hadidi, C.S. Pratt, M.P. Sealy, J.A. Turner, Ultrasonic mapping of hybrid additively manufactured 420 stainless steel, *Ultrasonics* 110 (2021), 106269, <https://doi.org/10.1016/j.ultras.2020.106269>.
- [29] A. Börger, P. Supancic, R. Danzer, The ball on three balls test for strength testing of brittle discs: stress distribution in the disc, *J. Eur. Ceram. Soc.* 22 (2002) 1425–1436, [https://doi.org/10.1016/S0955-2219\(01\)00458-7](https://doi.org/10.1016/S0955-2219(01)00458-7).
- [30] A. Börger, P. Supancic, R. Danzer, The ball on three balls test for strength testing of brittle discs: Part II: analysis of possible errors in the strength determination, *J. Eur. Ceram. Soc.* 24 (2004) 2917–2928, <https://doi.org/10.1016/j.jeurceramsoc.2003.10.035>.
- [31] *Advanced technical ceramics - Monolithic ceramics - Mechanical tests at room temperature - Part 5: Statistical analysis*, 1997.
- [32] S. Garner, E. Ruiz, J. Strong, A. Zavaliangos, Mechanisms of crack formation in die compacted powders during unloading and ejection: An experimental and modeling comparison between standard straight and tapered dies, *Powder Technol.* 264 (2014) 114–127, <https://doi.org/10.1016/j.powtec.2014.04.086>.
- [33] G.D. Quinn, NIST recommended practice guide fractography of ceramics and glasses, *Natl. Inst. Stand. Technol.* (2016), <https://doi.org/10.6028/NIST.SP.960-16e2>.
- [34] S. Baruah, J. Dutta, Hydrothermal growth of ZnO nanostructures, *Sci. Technol. Adv. Mater.* 10 (2009), 013001, <https://doi.org/10.1088/1468-6996/10/1/013001>.
- [35] V. Gerbreders, M. Krasovska, E. Sledevskis, A. Gerbreders, I. Mihailova, E. Tamaniš, A. Ogurcovs, Hydrothermal synthesis of ZnO nanostructures with controllable morphology change, *CrystEngComm* 22 (2020) 1346–1358, <https://doi.org/10.1039/C9CE01556F>.
- [36] H. Aoji, H. Shiomi, Effects of aging conditions on the morphologies of ZnO particles synthesized under hydrothermal conditions from layered zinc hydroxide as a precursor derived from zinc acetate, *J. Asian Ceram. Soc.* 8 (2020) 81–93, <https://doi.org/10.1080/21870764.2019.1709692>.
- [37] A.V. Smirnov, M.V. Korniyushin, A.A. Kholodkova, S.A. Melnikov, A.D. Stepanov, E. V. Fesik, Y.D. Ivakin, Cold sintering process of zinc oxide ceramics: powder preparation and sintering conditions effects on final microstructure, *Inorganics* 10 (2022) 197, <https://doi.org/10.3390/inorganics10110197>.
- [38] F.M. Mahoney, M.J. Readey, Ceramic compaction models: Useful design tools or simple trend indicators? *Cincinnati, OH (U. S.)* (1995). (<https://www.osti.gov/biblio/100304>).
- [39] R. Maier, *Ceramic Additive Manufacturing: New Insights Into Direct-Ink Writing and Cold Sintering*, 2022. <https://ceramics.org/event/46th-international-conference-and-expo-on-advanced-ceramics-and-composites>.
- [40] A.J. Allen, R.A. Maier, F. Zhang, I. Kuzmenko, J. Ilavsky, In situ microstructure characterization of potassium di-phosphate (KDP) densification during cold sintering, *Appl. Sci.* 12 (2022) 10493, <https://doi.org/10.3390/app122010493>.